Spin Reorientation in Antiferromagnetic Layered FePt$_5$P

Xin Gui,[1] Madalynn Marshall,[2,3] Ranuri S. Dissanayaka Mudiyanselage,[2] Ryan A. Klein,[4,5] Qiang Chen,[6] Qiang Zhang,[3] William Shelton,[7] Haidong Zhou,[6] Craig M. Brown,[4] Huibo Cao,[3] Martha Greenblatt,[2] Weiwei Xie[2]*

1. Department of Chemistry, Princeton University, Princeton, NJ, 08544, USA

2. Department of Chemistry and Chemical Biology, Rutgers University – New Brunswick, Piscataway, NJ, 08854, USA

3. Neutron Scattering Division, Oak Ridge National Laboratory, Oak Ridge, TN. 37831, USA.

4. NIST Center for Neutron Research, National Institute of Standards and Technology, Gaithersburg, MD, 20899, USA

5. Materials, Chemical, and Computational Sciences Directorate, National Renewable Energy Laboratory, Golden, CO, 80401, USA

6. Department of Physics, University of Tennessee, Knoxville, Tennessee 37996, USA

7. Cain Department of Chemical Engineering, Louisiana State University, Baton Rouge, LA 70803, USA

ABSTRACT

FePt$_5$P, a new substitutional variant of the CeCoIn$_5$ structure type in space group *P*4/*mmm*, was synthesized by high-temperature solid-state method and structurally characterized by X-ray diffraction. FePt$_5$P contains layers of FePt$_{12}$ clusters formed by magnetically active Fe, and heavy Pt with strong spin-orbit coupling (SOC); the layers are separated by P atoms. The various Fe-Pt distances in FePt$_{12}$ clusters generate complex magnetic orders in FePt$_5$P. According to temperature-dependent magnetic and specific heat measurements, FePt$_5$P shows a stripe-type antiferromagnetic order at T$_N$ ~ 90 K, which is also confirmed by resistivity measurements. Moreover, a spin reorientation occurs at ~ 74 K and ~ 68 K in and out of the *ab*-plane based on the specific heat measurements. The temperature-dependent neutron powder diffraction patterns demonstrate the antiferromagnetic order in FePt$_5$P, and the spins orientate up to 58.4° with respect to the *c*-axis at 10 K. First principles calculations of FePt$_5$P show the band splitting at the Fermi level by strong spin-orbit coupling (SOC) and the *s-d* hybridization between P and Fe/Pt electrons enhance the structural stability and affect the magnetic ordering.

Introduction

Design and synthesis of magnetic materials with targeted tunable phenomena have been grand challenges in the materials community for decades. Applying structure-magnetism relationships for materials discovery is a widely used chemical rule. Intermetallic compounds with flexible stoichiometry and tunable valence electron counts are ideal platforms to study the structure-magnetism relationship, and to predict the magnetic properties, for example, in the itinerant magnets $Ti_3Co_5B_2$-type[1–4] and $AlCo_2B_2$-type[5,6] structures.[7,8]

Recently, we discovered a new family of compounds with $MgPt_5As$-type structure, such as the rare-earth-free ferromagnetic (FM) $MnPt_5As$, antiferromagnetic (AFM) $MnPt_5P$ and $YbPt_5P$.[9–11] These new compounds exhibit various magnetic behaviors ranging from ferromagnetism and antiferromagnetism due to complex atomic interactions between magnetically active elements (Mn and Yb) separated by non-magnetic stacking layers.

One approach by Solid-State chemists to tune magnetic ordering in new phases is to adjust the valence electron count. s. However, the magnetic states in materials can also be manipulated and detected by introducing elements with strong spin-orbit coupling (SOC) on non-magnetic sites. For example, non-magnetic noble metals with large SOC including Rh, Pt, and W have been shown to tune the spin orientation.[12] Moreover, SOC effects in magnetic materials is crucial for other spin-transfer effects, such as spin penetration length[13–14], giant magnetoresistance (GMR)[15] and enhanced spin pumping.[16] When SOC effect from Ir/Pt/Au is coupled with $3d$ electrons from Mn, the appearance of GMR and anisotropic magnetoresistance (AMR) is appreciable, as in MnX.[17–21] In addition, the thickness of the antiferromagnetic layers is a key factor to tune the magnitude of existing spin-transfer effects.[22–25]

Herein, a new bulk AFM material $FePt_5P$ that couples a layered structure with strong SOC was discovered and synthesized. $FePt_5P$ crystallizes with a layered structure, analogous to the well-known layered heavy-fermion superconductor, $CeCoIn_5$.[26,27] With the high concentration of Pt per formula unit, it is expected that strong SOC effect are introduced by the Pt atoms. The $FePt_{12}$ polyhedral layers are separated by P layers in $FePt_5P$. Such polyhedral clusters are also found in AFM $FePt_3$ consisting of similar $FePt_{12}$ polyhedra.[28,29] Neutron powder diffraction measurements show a clear AFM ordering transition at $T_N \sim 90$ K. Spin reorientations were observed at lower temperatures, ~ 68 K and ~ 74 K along the c-axis and in the ab-plane,

respectively. Large magnetoresistance at 9 T ($\Delta\rho/\rho_0 \sim 35$ %) at 1.7 K is found by field-dependent resistivity measurements, which is frequently observed in AFM spintronic candidates.[22] First-principles calculations indicates that the SOC and AFM ordering significantly affect the electronic structures near the Fermi energy in $FePt_5P$.

Experimental Section

Sample preparation: $FePt_5P$ can be synthesized *via* a high-temperature solid-state method. The mixture of Fe powder (-200 mesh, 99+%, Alfa Aesar), Pt powder (-22 mesh, 99.99%, BTC) and red P powder (-100 mesh, 99%, BTC) were thoroughly mixed with a molar ratio of 1: 5: 1. [#] The mixture was pressed into a solid pellet. The pellet was placed into an alumina crucible and then sealed into an evacuated silica tube ($< 10^{-5}$ torr). The sealed tube was slowly heated up to 1050 °C at a rate of 30 °C per hour to prevent phosphorus from exploding. After annealing at 1050 °C for two days, the sample was slowly cooled down to room temperature in ten days. The polycrystalline $FePt_5P$ is obtained by this process. Small single crystals (~$0.8 \times 0.8 \times 0.2$ mm^3) are found to be detachable from the sample bulk. The material is stable in the ambient air and humidity.

Phase Identification: To determine the phase purity, the room temperature powder X-ray diffraction (PXRD) pattern was collected on a Rigaku MiniFlex 600 powder X-ray diffractometer with Cu Kα radiation (λ = 1.5406 Å, Ge monochromator). The experiment was performed with 2θ angle between 5° and 90° with a step of 0.005° at a rate of 0.1°/min. Rietveld fitting on FullProf Suite was employed to obtain the weight percentage of obtained phases.[30] The temperature-dependent PXRD patterns were measured every 10 K from 300 to 10 K with a HUBER X-Ray Diffractometer equipped with Helium-cryogenic. The LeBail refinement was performed on each pattern to obtain the phase information and accurate lattice parameters.[31,32]

Structure Determination: The crystal structure of $FePt_5P$ was determined using a Bruker Apex II Single Crystal X-ray Diffractometer equipped with Mo radiation ($\lambda_{K\alpha}$= 0.71073 Å) at room temperature. To ensure the homogeneity, multiple pieces of crystals (~$15 \times 50 \times 50$ μm^3) from different batches were measured. The crystals were mounted on a Kapton loop and protected by glycerol. Four different crystal and detector orientations were generated to take the measurement with an exposure time of 10 seconds per frame. The scanning 2θ width was set to 0.5°. Direct methods and full-matrix least-squares on F^2 models within the *SHELXTL* package were applied to solve the structure.[33] Data acquisition was obtained *via* Bruker *SMART* software with the corrections on Lorentz and polarization effect done by *SAINT* program. Numerical absorption corrections were accomplished with *XPREP*.[33,34]

Neutron Powder Diffraction (NPD): Neutron powder diffraction patterns were collected on the time-of-flight (TOF) powder diffractometer (POWGEN) at the Spallation Neutron Source (SNS) at Oak Ridge National Laboratory (ORNL). The measurement was carried out at various temperatures at T= 10, 71, 80, 100, and 150 K using a neutron wavelength band of 0.97−2.033 Å with a central wavelength of 1.5 Å. A powder sample of ~3g was loaded into a 6 mm diameter vanadium sample can with a copper gasket. FullProf refinement suite and Sarah programs were used to solve the nuclear and magnetic structure.[30,32,35]

Scanning Electron Microscope (SEM): The chemical compositions were confirmed using a high vacuum scanning electron microscope (SEM) (JSM-6610 LV). Samples were placed on carbon tape prior to loading into the SEM chamber and were examined at 20 kV.

Physical Properties Measurements: Magnetic properties, resistivity and heat capacity measurements were performed on a Quantum Design Dynacool Physical Property Measurement System (PPMS) with the temperature ranging from 1.8 to 300 K with and without applied fields up to 9 T. The magnetic susceptibility is defined as χ = M/H. Here, M is the magnetization in units of emu, and H is the applied magnetic field. A standard relaxation calorimetry method was used to measure heat capacity and the data were collected in zero magnetic field between 1.8 K and 220 K using N-type grease. All the measurements were performed on manually picked single crystal samples of $FePt_5P$.

Electronic Structure Calculations: The band structure and density of states (DOS) of $FePt_5P$ were calculated using the WIEN2k program, which has the full-potential linearized augmented plane wave method (FP-LAPW) with local orbitals implemented.[36] The electron exchange-correlation potential was used to treat the electron correlation within the generalized gradient approximation, which is parameterized by Perdew et. al.[37] The conjugate gradient algorithm was applied, and the energy cutoff was set at 500 eV. Reciprocal space integrations were completed over an 8×8×4 Monkhorst-Pack k-points mesh for non-magnetic calculation and 3×12×4 for magnetic calculation.[38] With these settings, the calculated total energy converged to less than 0.1 meV per atom. The spin-orbit coupling (SOC) effects were only applied for Pt atoms. The structural lattice parameters obtained from single crystal X-ray diffraction (SC-XRD) are used for both calculations for non-magnetic calculation while for magnetic calculation; the magnetic structure obtained from NPD was utilized.

Results and Discussion

Crystal Structure and Phase Determination of FePt$_5$P: The crystal structure of FePt$_5$P determined by the single crystal XRD is shown in Figure 1*a*. The crystallographic data, including atomic coordinates, site occupancies, and equivalent isotropic thermal displacement parameters are listed in Tables 1 and 2. As can be seen in Figure 1*a*, FePt$_5$P adopts a layered tetragonal structure with the space group *P*4/*mmm*. In FePt$_5$P, the face-sharing FePt$_{12}$ polyhedral cluster layers are separated by P layers. By comparing with the crystal structure of binary FePt$_3$ also shown in Figure 1*a*, it is seen that similar FePt$_{12}$ polyhedron exists in FePt$_3$.[29,39] The Fe-Pt bonding within the *ab*-plane (2.757 (1) Å) is shorter than that out of the *ab*-plane (2.776 (1) Å), which are slightly shorter than Fe-Pt bond lengths in FePt$_3$ (2.738 (1) Å). The significant difference between FePt$_5$P and FePt$_3$ is the Fe-Fe distance, which doubles in FePt$_5$P along *c*-axis, and which contributes to the magnetic anisotropy in FePt$_5$P. The SEM image of the FePt$_5$P chunk is shown in Figure 1*b* where the layered structural feature is easily observed.

The phase purity of polycrystalline FePt$_5$P was examined by PXRD at 300 K. The Rietveld refined powder pattern is shown in Figure 1*c*. FePt$_3$ and Pt were included into the refinement as the impurities. According to the results, the weight percentages of FePt$_3$ and Pt are 3.72 (6) wt% and 0.09 (3) wt%, respectively. The refinement results, R_p, R_{wp} and χ^2, are 7.87, 10.2 and 2.65, respectively, which indicate a reasonable PXRD refinement.
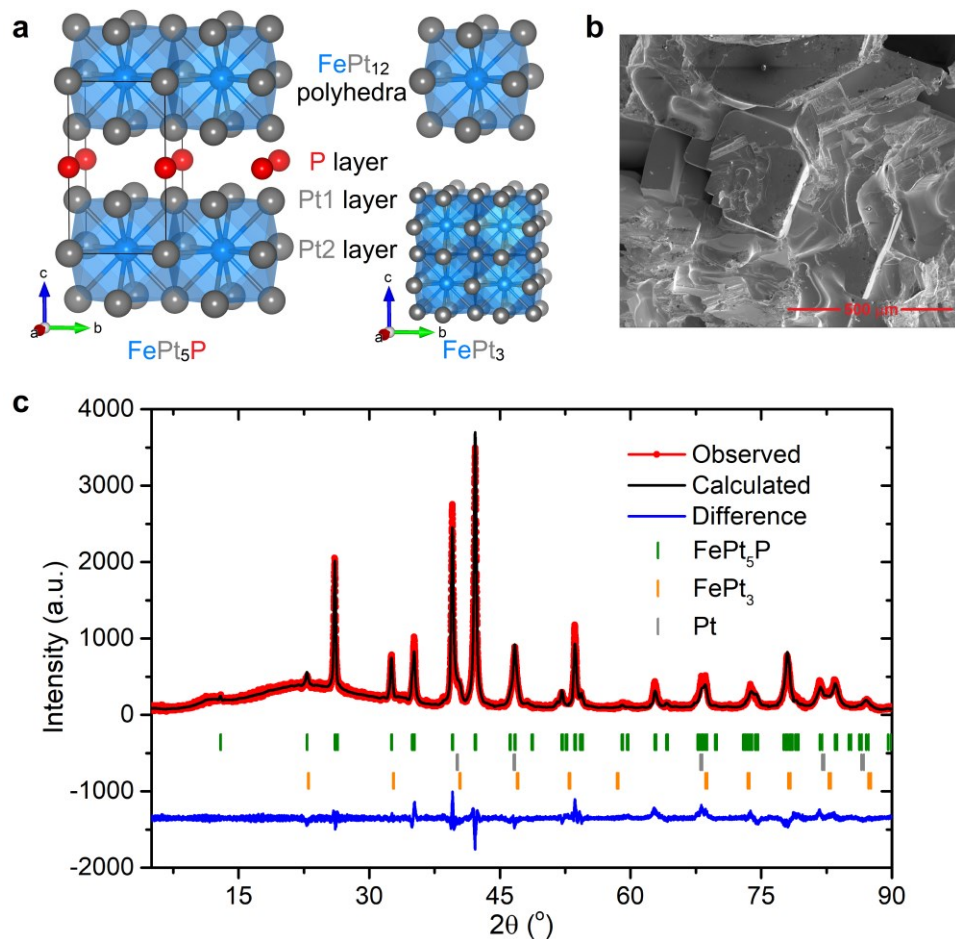
Figure 1. *a.* Crystal structure of FePt$_5$P and FePt$_3$. Blue, grey and red balls represent Fe, Pt and P atoms, respectively. *b.* The SEM picture of polycrystalline FePt$_5$P with layered feature. *c.* Powder XRD pattern with Rietveld fitting of polycrystalline FePt$_5$P. The red line with ball indicates the observed pattern, the black line represents the calculated pattern of FePt$_5$P, and the green line stands for the residual intensities. The Bragg peak positions of different phases are indicating by the vertical ticks.

Table 1. Single crystal structure refinement for FePt$_5$P at 296 (2) K. (Values in parentheses indicate one standard deviation.)

Refined Formula	FePt$_5$P
F.W. (g/mol)	1062.27
Space group; Z	*P* 4/*mmm*; 1
a(Å)	3.899 (2)
c(Å)	6.852 (3)
V (Å^3)	104.18 (9)

θ range (º)	2.973-33.150
No. reflections; R_{int}	1239; 0.0365
No. Independent reflections	153
No. parameters	12
R_1: ωR_2 ($I > 2\delta(I)$)	0.207; 0.0484
Goodness of fit	1.100
Diffraction peak and hole (e$^-$/ Å^3)	6.628; -2.341

Table 2. Atomic coordinates and equivalent isotropic displacement parameters for FePt$_5$P at 296 (2) K. (U_{eq} is defined as one-third of the trace of the orthogonalized U_{ij} tensor (Å^2)) (Values in parentheses indicate one standard deviation.)

Atom	Wyckoff.	Occ.	x	y	z	U_{eq}
Pt1	4i	1	0	½	0.2885 (1)	0.0067 (2)
Pt2	1a	1	0	0	0	0.0065 (2)
Fe3	1c	1	½	½	0	0.0075 (7)
P4	1b	1	0	0	½	0.007 (1)

Magnetic Properties of Single Crystal FePt$_5$P: Magnetic properties of FePt$_5$P were measured on the small single crystals manually selected (size ~ 0.2 mm) and pre-aligned by single crystal X-ray diffraction before loading into the PPMS. The single crystals are sequentially aligned with two different orientations: the external magnetic field is first perpendicular (B⊥c) and then parallel to the c-axis (B//c) in two separate measurements. The results of temperature-dependence of magnetic susceptibility are presented in Figure 2 with an applied magnetic field of 1000 Oe. The magnetic susceptibility shows an upturn starting from 200 K, and as the temperature decreases, the magnetic susceptibility increases and reaches a plateau below ~ 90 K. Similar magnetic behaviors are seen by both Zero-Field Cooling (ZFC) and Field Cooling (FC) in Figure S1. When the applied magnetic field was parallel to the c axis, the magnitude of magnetic susceptibility is nearly identical, but with a slightly smaller value in the high temperature region (> 200 K), which implies a small magnetic anisotropy. The hysteresis loop of FePt$_5$P is shown in Figure 3. The results from both applied magnetic field directions imply soft magnetic behavior. Weak magnetic anisotropy is observed. Interestingly, when the applied magnetic field is perpendicular to the c-axis, the magnetization of the sample shows a small saturated moment of ~ 0.010 μ$_B$/Fe in Figure 3a after subtracting the FePt$_3$'s magnetic

contribution. However, the hysteresis loop of FePt$_5$P with applied magnetic field parallel to the c-axis doesn't have a saturated moment at 300 K. Moreover, when the sample was cooled down, both orientations displayed larger absolute values of the slope down to 90 K where the magnetizations at 9 T reached its maxima. After the temperature was decreasing to below 90 K, i.e., 80 K, the absolute value of the slope dropped along with the decreasing of magnetization value. This indicated another magnetic ordering of FePt$_5$P occurs near 90 K.
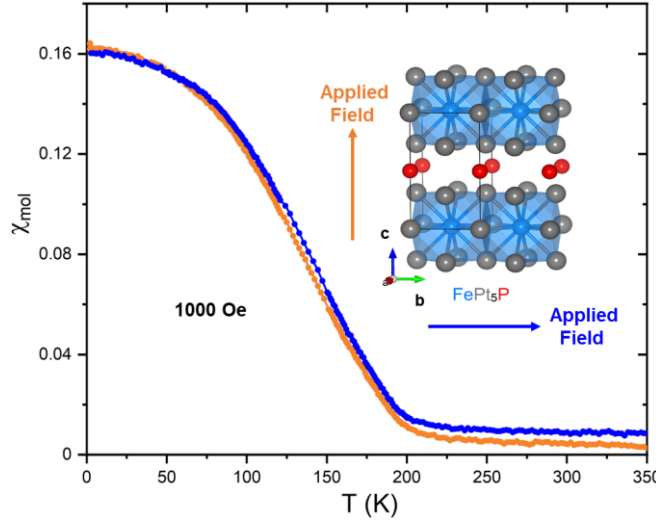
Figure 2. Temperature-dependence of magnetic susceptibility of FePt$_5$P crystals with magnetic field applied (Blue: parallel to c-axis; Orange: perpendicular to c-axis) from 1.8 K to 350 K.
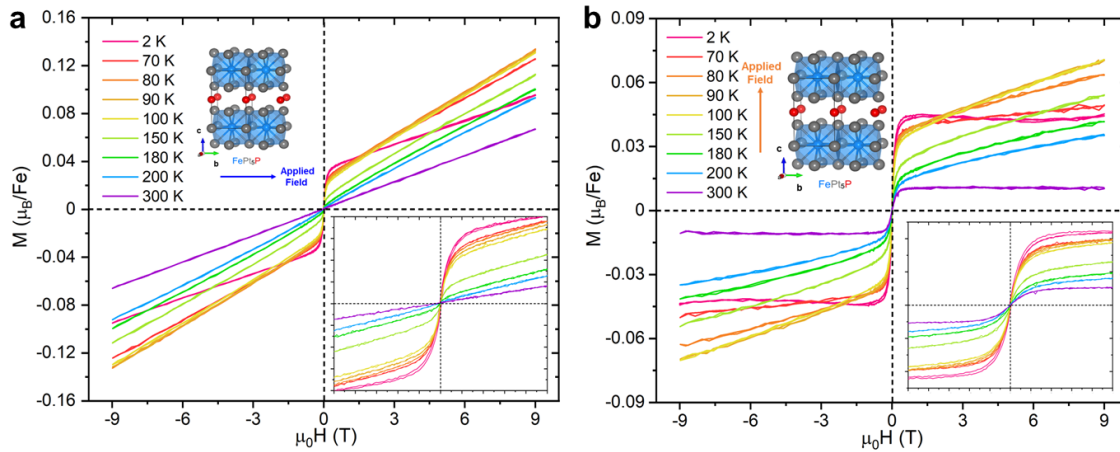

Figure 3. Hysteresis loops of FePt$_5$P at various temperatures with an external magnetic field from -9 T to 9 T. **a.** parallel to c-axis; **b.** perpendicular to c-axis. The inset of figures shows the enlarged figure at a low field range between -1 and 1 T.

9

Magnetic Structure of FePt₅P: Time-of-flight (TOF) neutron powder diffraction (NPD) data was collected at POWGEN (Oak Ridge National Laboratory) to determine the magnetic structures of FePt₅P at various temperatures. Figure 4*a* shows the refined neutron diffraction patterns measured at 150, 80 and 10 K. Two impurity phases are identified in the sample including FePt₃ and Pt, which is consistent with PXRD results. The crystal structures of FePt₅P, FePt₃ and Pt reproduce well the peaks observed at 180 and 300 K, as shown in Figure S2. The analysis of NPD data further confirms the tetragonal *P4/mmm* structure of FePt₅P, in agreement with the PXRD results. The minor peaks not included in the refinements are also examined and compared at all the temperatures. It can be concluded that the minor peaks present are not temperature dependent and have no contribution to the magnetic phases of FePt₅P. Above 150 K, the magnetic reflections can be indexed with a propagation vector $k = (\frac{1}{2}, \frac{1}{2}, 0)$, belonging to the FePt₃ phase.[28,40] Further cooling down to 80 K, additional magnetic reflections are observed associated with the AFM order in FePt₅P, as shown in Figure 3b. These magnetic reflections can be indexed with the propagation vector $k = (\frac{1}{2}, 0, 0)$. The magnetic peaks from typical lattice planes of FePt₅P ((0 0 0), (0 0 1), (-1 0 1), (0 1 0)) were gradually suppressed when the temperature was increased up to 100 K. The refinement using the unit cell, $2a \times b \times c$ revealed FePt₅P to have a stripe-type AFM ordering with magnetic space group P_amma (#51.298) including FM *bc* planes coupled AFM along the *a* axis. NPD measurements performed at 70 K consist of similar magnetic reflections as at 80 K. Thus, the ordered moments are 2.2 (2) μ_B/Fe and 2.8 (1) μ_B/Fe at 80 K and 70 K, respectively. A second magnetic transition of FePt₃ also occurs at 80 K and was indexed using the k vector $(0, 0, \frac{1}{2})$.[29] The magnetic structure of FePt₃ has a stripe-type AFM ordering along the *a* axis with an ordered moment of 1.01 (43) μ_B/Fe at 80 K. The NPD data collected at 10 K, reveals no new reflections, however, a rotated AFM axis for FePt₅P is observed. The resulting ordered moment for this state was determined to have the components $m_a = 3.0$ (2) μ_B/Fe and $m_c = 1.8$ (3) μ_B/Fe with a total ordered moment of $m_{tot} = 3.5$ (3) μ_B/Fe. Considering the ordered moments along the *a* and *c* directions, the rotated angle of the AFM axis was calculated to deflect towards the *c* axis and determined to be ~58.4°. The magnetic structures for FePt₅P, with and without spin reorientations, are shown in Figure 4 *c & d*.
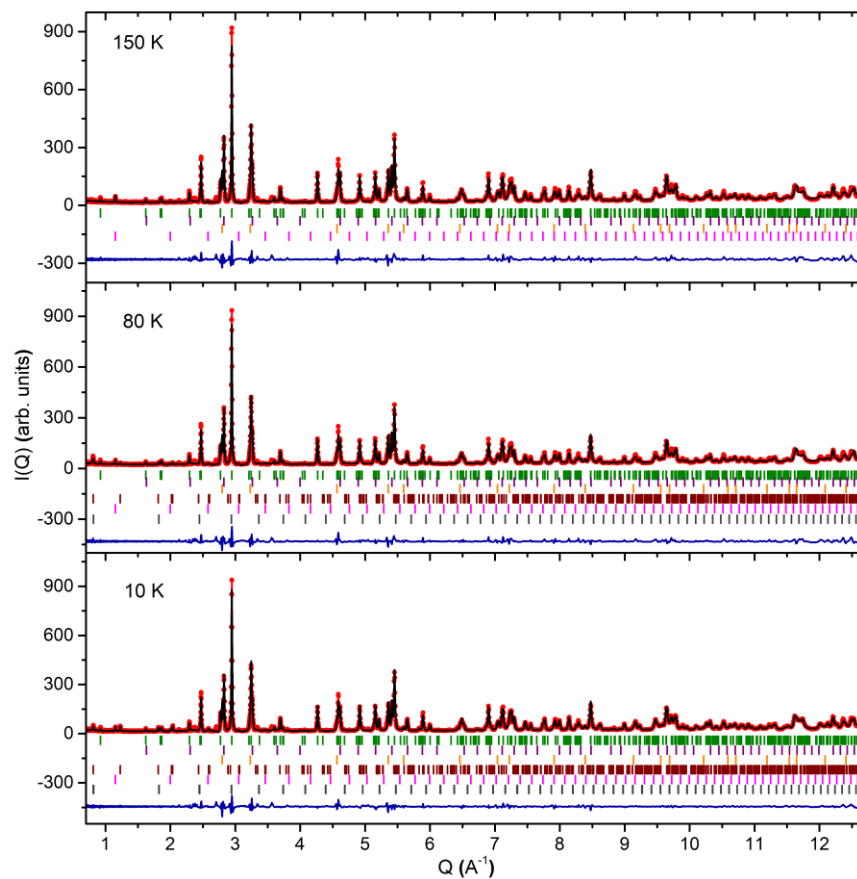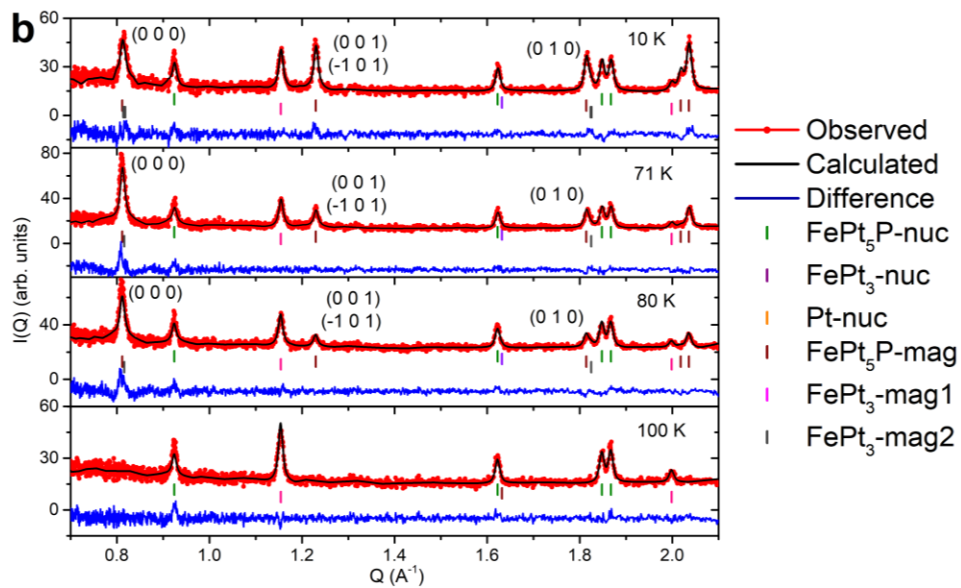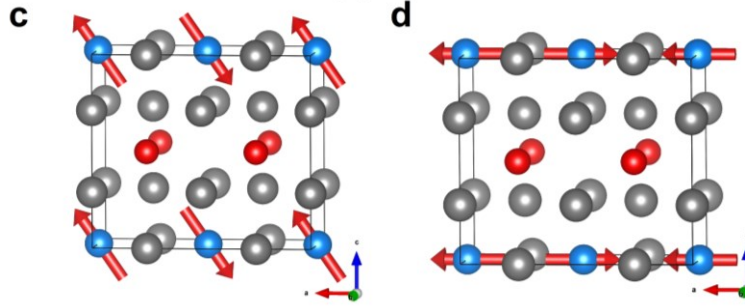
Figure 4. *a.* The refined neutron powder diffraction patterns at 150 K, 80 K, and 10 K. ***b.*** The enlarged low-Q region for refined patterns at 10 K, 71 K, 80 K and 100 K. The lattice plane marked on the figure indicate where the magnetic peaks were originating. ***c.*** The magnetic structure of $FePt_5P$ refined from NPD. ***d.*** Hypothetical magnetic structure without spin reorientation for theoretical calculations.

Resistivity and Heat Capacity of $FePt_5P$ crystals: Four-probe method was applied to measure the resistivity on one of the larger pieces of crystals used in magnetic properties measurements. The temperature-dependence of resistivity under five different magnetic field, 0, 0.5, 1, 5 and 9 T, are presented in Figure 5a. The resistivity of $FePt_5P$ showed similar linear $\rho(T)$ behavior above ~118 K in all cases, as fitted by the white line, except the one measured under 1 T where a kink was observed around 300 K. The resistivity started to increase when the temperature dropped below ~118 K and reached a maximum at ~86 K. Based on the NPD results, that the magnetic ordering of $FePt_5P$ starts between 80 and 100 K, the increasing $\rho(T)$ at ~118K could be due to the small amount of ordered $FePt_3$ impurity scattering the electrons of $FePt_5P$. Moreover, the subsequent drop of resistivity can be interpreted as the *s-d* electron scattering based on its T^3 behavior when fitted to $\rho(T) = \rho_0 + AT^n$ where ρ_0 is the residual resistivity due to defect scattering; A is a constant and n is an integer determined by the interaction pattern. The magnetoresistance of $FePt_5P$ displayed in Figure S4 implies that ~35% magnetoresistance can be observed at 1.7 K at an applied magnetic field of 9 T. With increasing temperature, the large magnetoresistance was suppressed gradually (Fig. S4).
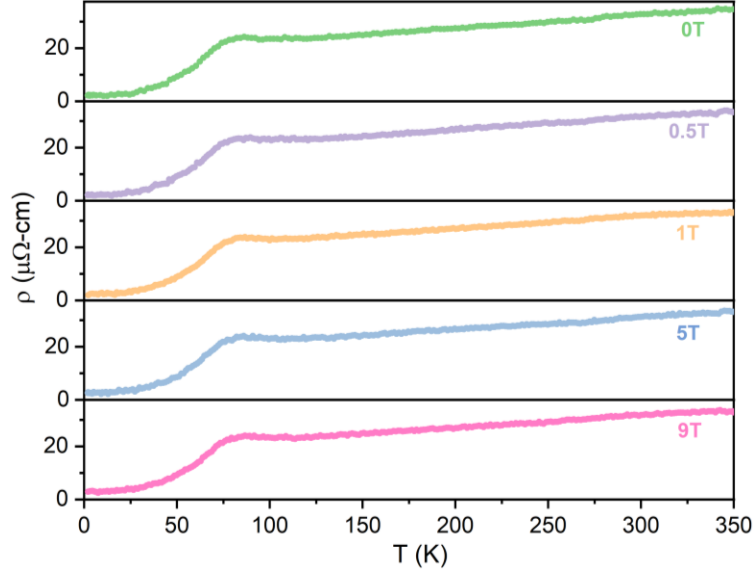
Figure 5. Temperature-dependence of resistivity measured between 1.7 K and 350 K under different external magnetic fields (0, 0.5, 1, 5 and 9 T).

Heat capacity measurement made on the same piece of crystal used in the resistivity measurement was performed without an applied magnetic field and the result is presented in Figure 6. Four peaks are observed within the explored temperature range (1.8 K to 225 K) at around 170, 89, 74 and 68 K. Based on previous results, the smaller peak around 170 K ($\Delta C \sim$ 3.5 J mol^{-1} K^{-1}) can be attributed to the magnetic ordering of FePt$_3$ impurity, which is consistent with the suggested reason of resistivity increasing after 118 K. The heat capacity jump of the other three peaks are ~7.0 J mol^{-1} K^{-1} (~89 K), ~3.0 J mol^{-1} K^{-1} (~74 K) and ~4.2 J mol^{-1} K^{-1} (~68 K). According to the NPD results, the three peaks at 89 K, 74 and 68 K reflect the entropy changes of the AFM transitions and spin reorientations along different directions of FePt$_5$P, respectively. The the specific heat peak at 170 K is consistent with the magnetic reflections observed in the NPD at 150 K, which stem from the AFM transition of FePt$_3$.[29,39]
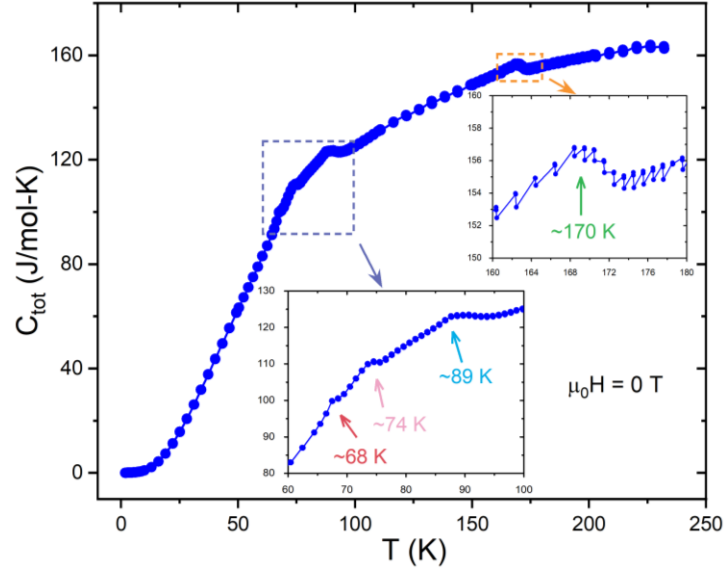
Figure 6. Heat capacity of FePt$_5$P crystal between 1.8 K and 225 K without an applied magnetic field. The insets show the enlarged picture of entropy change regions.

Electronic Structure of FePt$_5$P: The band structures calculated for FePt$_5$P are shown in Figure 7a. The projection of significant orbitals for each atomic site is also given in Figure S5. Spin-orbit coupling (SOC) effect from Pt and spin polarization (SP) from Fe were taken into account and the comparison among band structures with/without those effects were also calculated. In the left two figures of Figure 7a, the band structures with/without consideration of SOC effect are given, where the Brillouin Zone (BZ) was generated from the original unit cell. Some of the bands around the Fermi level are split and lead to bandgaps, such as the bands from ~ -0.05 ~ to ~0.1 eV between Γ and X points. New saddle points are observed near the E$_F$ when SOC is included, such as at the M point (Fig. 7a). When including both SOC and SP, with the type of atoms and construction of BZ are shown in Figure 7c, the density of bands near E$_F$ is less dense compared with the one where only the SOC effect is considered. Less saddle points can also be seen at the Fermi level (with SOC and SP), which indicates a more stable state for FePt$_5$P. The contribution of both SOC and SP to stability of FePt$_5$P is recognized intuitively by Figure 7b which list the density of states (DOS) corresponding to band structures in figure 7a. It is clear in Figure 7b that the DOS at E$_F$ decreases dramatically with SOC and SP included. Moreover, the E$_F$ in the SOC+SP case is moving towards a pseudo gap at ~ -0.2 eV. The Fe-d orbitals have the

14

largest contribution at the Fermi energy, far larger than that of Pt and P atoms, which is also displayed in Figure S6.
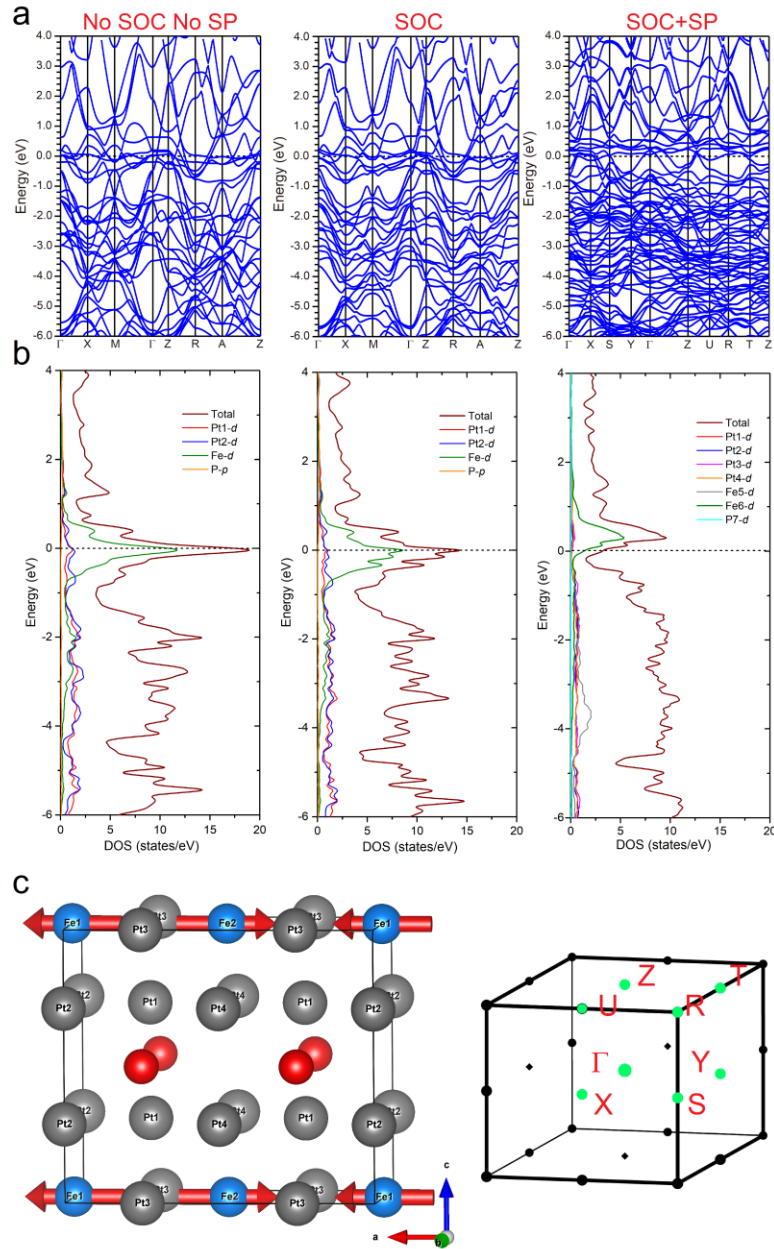

Figure 7. *a.* Band structures of FePt$_5$P with/without consideration of SOC effect and SP. ***b.*** Density of states of FePt$_5$P corresponding to ***a***. ***c.*** Magnetic unit cell and Brillouin Zone of magnetically ordered FePt$_5$P.

Conclusion

In this paper, we designed and synthesized the first ternary compound in the Fe-Pt-P system, FePt$_5$P, crystallizes in a layered tetragonal structure in the space group of $P4/mmm$, which orders antiferromagnetically along the c direction of the unit cell below $T_N \sim 90$ K. The spins are reoriented below ~ 68 K. Resistivity measurements indicate metallic behavior and the dominance of s-d scattering below T_N. First principles calculations of electronic structure show s-d electronic interaction governing the resistivity in FePt$_5$P, which is heavily influenced by the effect of SOC and magnetism. The new material serves as an ideal model for the investigation of the relationship of magnetism, structure and spin-orbit coupling in low-dimensional correlated electronic phases with constituent atoms of coupled magnetic and spin orbit couple properties, respectively.

Certain commercial equipment, instruments, or materials (or suppliers, or software, ...) are identified in this paper to foster understanding. Such identification does not imply recommendation or endorsement by the National Institute of Standards and Technology, nor does it imply that the materials or equipment identified are necessarily the best available for the purpose.

Supporting Information

Supplementary information, details of author contributions and competing interests; and statements of data are available at https://doi.org/xxx including:

Magnetic structure of FePt$_3$ at 150 K; Low-temperature PXRD; Lattice parameters and volume of FePt$_5$P unit cell changes; Magneto-resistivity at various temperatures; Projection of orbitals from Fe, Pt and P atoms on band structure; Table of Rietveld refinement reliability factors.

Acknowledgements

Reference

(1)   Burghaus, J.; Dronskowski, R.; Miller, G. J. Slater–Pauling Behavior within Quaternary Intermetallic Borides of the $Ti_3Co_5B_2$ Structure-Type. *J. Solid State Chem* **2009**, *182* (10), 2613–2619.

(2)   Shankhari, P.; Scheifers, J. P.; Hermus, M.; Yubuta, K.; Fokwa, B. P. T. Unexpected Trend Deviation in Isoelectronic Transition Metal Borides $A_3T_5B_2$ (A = Group 4, T = Group 9): $Ti_3Co_5B_2$- vs. Perovskite-Type Studied by Experiments and DFT Calculations. *Z Anorg Allg Chem.* **2017**, *643* (21), 1551–1556.

(3)   Shankhari, P.; Zhang, Y.; Stekovic, D.; Itkis, M. E.; Fokwa, B. P. T. Unexpected Competition between Antiferromagnetic and Ferromagnetic States in $Hf_2MnRu_5B_2$: Predicted and Realized. *Inorg. Chem.* **2017**, *56* (21), 12674–12677.

(4)   Zhang, Y.; Miller, G. J.; Fokwa, B. P. T. Computational Design of Rare-Earth-Free Magnets with the $Ti_3Co_5B_2$-Type Structure. *Chem. Mater.* **2017**, *29* (6), 2535–2541.

(5)   Chai, P.; Stoian, S. A.; Tan, X.; Dube, P. A.; Shatruk, M. Investigation of Magnetic Properties and Electronic Structure of Layered-Structure Borides AlT_2B_2 (T=Fe, Mn, Cr) and $AlFe_{2-x}Mn_xB_2$. *J. Solid State Chem.* **2015**, *224*, 52–61.

(6)   Tan, X.; Chai, P.; Thompson, C. M.; Shatruk, M. Magnetocaloric Effect in $AlFe_2B_2$: Toward Magnetic Refrigerants from Earth-Abundant Elements. *J. Am. Chem. Soc.* **2013**, *135* (25), 9553–9557.

(7)   Kovnir, K.; Reiff, W. M.; Menushenkov, A. P.; Yaroslavtsev, A. A.; Chernikov, R. V.; Shatruk, M. "Chemical Metamagnetism": From Antiferromagnetic $PrCo_2P_2$ to Ferromagnetic $Pr_{0.8}Eu_{0.2}Co_2P_2$ via Chemical Compression. *Chem. Mater.* **2011**, *23* (12), 3021–3024.

(8)   Kovnir, K.; Thompson, C. M.; Zhou, H. D.; Wiebe, C. R.; Shatruk, M. Tuning Ferro- and Metamagnetic Transitions in Rare-Earth Cobalt Phosphides $La_{1-x}Pr_xCo_2P_2$. *Chem. Mater.* **2010**, *22* (5), 1704–1713.

(9)   Gui, X.; Xie, W. Crystal Structure, Magnetism, and Electronic Properties of a Rare-Earth-Free Ferromagnet: $MnPt_5As$. *Chem. Mater.* **2020**, *32* (9), 3922–3929.

(10) Gui, X.; Chang, T.-R.; Wei, K.; Daum, M. J.; Graf, D. E.; Baumbach, R. E.; Mourigal, M.; Xie, W. A Novel Magnetic Material by Design: Observation of Yb^{3+} with Spin-1/2 in Yb_xPt_5P. *ACS Cent. Sci.* **2020**, *6* (11), 2023–2030.

(11) Gui, X.; Klein, R. A.; Brown, C. M.; Xie, W. Chemical Bonding Governs Complex Magnetism in $MnPt_5P$. *Inorg. Chem.* **2021**, *60* (1), 87–96.

(12) Gambardella, P., Miron, I.M. Current-induced spin–orbit torques. *Philos. Trans. R. Soc. A* **2011**, *369*(1948), 3175-3197.

(13) Acharyya, R.; Nguyen, H. Y. T.; Pratt, W. P.; Bass, J. A Study of Spin–Flipping in Sputtered IrMn Using Py-Based Exchange-Biased Spin-Valves. *J. Appl. Phys.* **2011**, *109* (7), 07C503.

(14) Merodio, P.; Ghosh, A.; Lemonias, C.; Gautier, E.; Ebels, U.; Chshiev, M.; Béa, H.; Baltz, V.; Bailey, W. E. Penetration Depth and Absorption Mechanisms of Spin Currents in $Ir_{20}Mn_{80}$ and $Fe_{50}Mn_{50}$ Polycrystalline Films by Ferromagnetic Resonance and Spin Pumping. *Appl. Phys. Lett.* **2014**, *104* (3), 032406.

(15) Wang, Y.; Song, C.; Wang, G.; Miao, J.; Zeng, F.; Pan, F. Anti-Ferromagnet Controlled Tunneling Magnetoresistance. *Adv. Funct. Mater.* **2014**, *24* (43), 6806–6810.

(16) Frangou, L.; Oyarzún, S.; Auffret, S.; Vila, L.; Gambarelli, S.; Baltz, V. Enhanced Spin Pumping Efficiency in Antiferromagnetic IrMn Thin Films around the Magnetic Phase Transition. *Phys. Rev. Lett.* **2016**, *116* (7), 077203.

(17) Shick, A. B.; Khmelevskyi, S.; Mryasov, O. N.; Wunderlich, J.; Jungwirth, T. Spin-Orbit Coupling Induced Anisotropy Effects in Bimetallic Antiferromagnets: A Route towards Antiferromagnetic Spintronics. *Phys. Rev. B* **2010**, *81* (21), 212409.

(18) Park, B. G.; Wunderlich, J.; Martí, X.; Holý, V.; Kurosaki, Y.; Yamada, M.; Yamamoto, H.; Nishide, A.; Hayakawa, J.; Takahashi, H.; Shick, A. B.; Jungwirth, T. A Spin-Valve-like Magnetoresistance of an Antiferromagnet-Based Tunnel Junction. *Nat. Mater.* **2011**, *10* (5), 347–351.

(19) Wang, Y. Y.; Song, C.; Cui, B.; Wang, G. Y.; Zeng, F.; Pan, F. Room-Temperature Perpendicular Exchange Coupling and Tunneling Anisotropic Magnetoresistance in an Antiferromagnet-Based Tunnel Junction. *Phys. Rev. Lett.* **2012**, *109* (13), 137201.

(20)   Galceran, R.; Fina, I.; Cisneros-Fernández, J.; Bozzo, B.; Frontera, C.; López-Mir, L.; Deniz, H.; Park, K.-W.; Park, B.-G.; Balcells, L.; Martí, X.; Jungwirth, T.; Martínez, B. Isothermal Anisotropic Magnetoresistance in Antiferromagnetic Metallic IrMn. *Sci. Rep.* **2016**, *6* (1), 35471.

(21)   Wu, S. M.; Zhang, W.; KC, A.; Borisov, P.; Pearson, J. E.; Jiang, J. S.; Lederman, D.; Hoffmann, A.; Bhattacharya, A. Antiferromagnetic Spin Seebeck Effect. *Phys. Rev. Lett.* **2016**, *116* (9), 097204.

(22)   Zhang, W.; Jungfleisch, M. B.; Jiang, W.; Pearson, J. E.; Hoffmann, A.; Freimuth, F.; Mokrousov, Y. Spin Hall Effects in Metallic Antiferromagnets. *Phys. Rev. Lett.* **2014**, *113* (19), 196602.

(23)   Molina-Ruiz, M.; Lopeandía, A. F.; Pi, F.; Givord, D.; Bourgeois, O.; Rodríguez-Viejo, J. Evidence of Finite-Size Effect on the N'eel Temperature in Ultrathin Layers of CoO Nanograins. *Phys. Rev. B* **2011**, *83* (14), 140407.

(24)   Vallejo-Fernandez, G.; Fernandez-Outon, L. E.; O'Grady, K. Antiferromagnetic Grain Volume Effects in Metallic Polycrystalline Exchange Bias Systems. *J. Phys. D: Appl. Phys.* **2008**, *41* (11), 112001.

(25)   Saglam, H.; Zhang, W.; Jungfleisch, M. B.; Sklenar, J.; Pearson, J. E.; Ketterson, J. B.; Hoffmann, A. Spin Transport through the Metallic Antiferromagnet FeMn. *Phys. Rev. B* **2016**, *94* (14), 140412.

(26)   Movshovich, R.; Jaime, M.; Thompson, J. D.; Petrovic, C.; Fisk, Z.; Pagliuso, P. G.; Sarrao, J. L. Unconventional Superconductivity in $CeIrIn_5$ and $CeCoIn_5$: Specific Heat and Thermal Conductivity Studies. *Phys. Rev. Lett.* **2001**, *86* (22), 5152–5155.

(27)   Izawa, K.; Yamaguchi, H.; Matsuda, Y.; Shishido, H.; Settai, R.; Onuki, Y. Angular Position of Nodes in the Superconducting Gap of Quasi-2D Heavy-Fermion Superconductor $CeCoIn_5$. *Phys. Rev. Lett.* **2001**, *87* (5), 057002.

(28)   Bacon, G. E.; Crangle, J.; Sucksmith, W. Chemical and Magnetic Order in Platinum-Rich Pt + Fe Alloys. *Proc. Math. Phys. Sci.* **1963**, *272* (1350), 387–405.

(29)   Kohgi, M.; Ishikawa, Y. Magnetic Excitations in a Metallic Antiferromagnet $FePt_3$. *J. Phys. Soc. Jpn.* **1980**, *49* (3), 985–993.

(30)   Rodríguez-Carvajal, J. Recent Advances in Magnetic Structure Determination by Neutron Powder Diffraction. *Physica B: Condens. Matter* **1993**, *192* (1), 55–69.

(31)   Le Bail, A.; Duroy, H.; Fourquet, J. L. Ab-Initio Structure Determination of $LiSbWO_6$ by X-Ray Powder Diffraction. *Mater. Res. Bull.* **1988**, *23* (3), 447–452.

(32)   Dinnebier, R. E.; Billinge, S. J. L. Powder Diffraction: Theory and Practice; *R. Soc. Chem.*, **2008**.

(33)   Sheldrick, G. M. Crystal Structure Refinement with SHELXL. *Acta Cryst C* **2015**, *71* (1), 3–8.

(34)   Bruker, S. Bruker SMART (Version 5.625). *Bruker AXS Inc., Madison, Wisconsin, USA* **2001**.

(35)   Wills, A. S. A New Protocol for the Determination of Magnetic Structures Using Simulated Annealing and Representational Analysis (SARAh). *Physica B: Condens. Matter* **2000**, 276–278, 680–681.

(36)   Blöchl, P. E. Projector Augmented-Wave Method. *Phys. Rev. B.* **1994**, *50* (24), 17953.

(37)   Perdew, J. P.; Wang, Y. Accurate and Simple Analytic Representation of the Electron-Gas Correlation Energy. *Phys. Rev. B* **1992**, *45* (23), 13244–13249.

(38)   King-Smith, R. D.; Vanderbilt, D. Theory of Polarization of Crystalline Solids. *Phys. Rev. B* **1993**, *47* (3), 1651–1654.

(39)   Maat, S.; Hellwig, O.; Zeltzer, G.; Fullerton, E. E.; Mankey, G. J.; Crow, M. L.; Robertson, J. L. Antiferromagnetic Structure of $FePt_3$ Films Studied by Neutron Scattering. *Phys. Rev. B* **2001**, *63* (13), 134426.

(40)   Palaith, D.; Kimball, C. W.; Preston, R. S.; Crangle, J. Magnetic Behavior of the Pt+Fe System Near Pt_3Fe. *Phys. Rev.* **1969**, 178 (2), 795–799.